Stability of a jet in confined pressure-driven biphasic flows at low Reynolds number in various geometries

Pierre Guillot and Annie Colin*
Rhodia Laboratoire du Futur, Unité mixte Rhodia-CNRS, Université Bordeaux I, UMR 5258, 178 Avenue du Docteur Schweitzer, 33608 Pessac, France

Armand Ajdari
Laboratoire de Physico-Chimie Théorique, UMR CNRS-ESPCI 7083, 10 rue Vauquelin, 75231 Paris Cedex 05, France
(Received 15 February 2008; revised manuscript received 29 April 2008; published 17 July 2008)

We adress the question of the stability of a confined coflowing jet at low Reynolds number in various geometries. Our study is motivated by recent experiments in microfluidic devices. When immiscible fluids flow in microchannels, either monodisperse droplets or parallel flows are obtained depending upon the flow rate of the aqueous phase and the oil phase. In these experiments, the confining and the shape of the geometry play a fundamental role. In a previous paper [Guillot *et al.*, Phys. Rev. Lett **99**, 104502 (2007)], we analyzed the stability of the jet in the framework of the lubrication approximation at low Reynolds number in a cylindrical geometry, and we related the transition between the droplets regime and the jet regime to the absolute-convective transition of the Rayleigh plateau instability. In this work, the effect of the channel geometry and the jet position within the microfluidic device are discussed. New flow patterns are pointed out. Bidimensional jets are encountered in square and rectangular geometry. Contrary to jets occuring in circular geometry, these two-dimensional jets are absolutely stable. Focusing on situations where the inner fluid is more viscous than the outer one, we evidence a range of parameters where droplets are produced through a blocking and pinching mechanism. In this particular case, the flow is unstable, the growing perturbations are convected upstream. This induces the clogging of the channel by the internal phase and its pinching by the external one. In a future presentation we will give a comparison between this model and experimental data.

DOI: 10.1103/PhysRevE.78.016307 PACS number(s): 47.15.−x

I. INTRODUCTION

The breakup of a liquid jet injected in another immiscible liquid has been investigated extensively for more than a century since the pioneer work of Plateau in 1873 [1]. This huge activity is related to the large field of practical and industrial applications ranging from chemical process to ink jet printing, through spray atomization, emulsification process, and polymer extrusion, to name a few. Since the seminal work of Rayleigh in 1879 [2,3], who showed that inviscid cylindrical jets in air are unstable to disturbances of wavelength larger than the jet radius, many authors have highlighted aspects of the remarkably complex interplay of interfacial stress, surface tension, and inertial forces that rules jet break up. The subject has been reviewed recently by Lin [4], Lin and Reitz [5], and Eggers [6].

The theory of absolute and convective instabilities [7–11] provides a useful framework to apprehend break-up scenarios in flowing systems. Absolute instability corresponds to disturbances growing and propagating both in the downstream and upstream directions. A continuous jet cannot thus exist and typically, drops are released intermittently either right at the injection nozzle or at a finite distance from it to form a dripping jet. At the opposite limit of high velocity, when the fluid inertia effects become more important than the surface tension effects, the instability becomes convective corresponding to perturbations that propagate downstream while they grow, allowing for a long continuous fluid thread to persist. Several experimental studies support this picture and the link between the absolute-convective transition of the instability to the dripping-jetting transition in the observed spatiotemporal behavior of the biphasic flow [12–20].

In a previous work [21], we applied these considerations to biphasic flows in cylindrical microfluidic devices. In this work, we extend our analysis to microchannels of nonradially symmetric cross sections, for which both the dripping and the parallel flow regimes have been not only observed but also exhaustively used for various applications [22–35]. Square and rectangular geometries are the most common situations encountered in PDMS devices [36].

In Sec. II, we recall the analytical prediction for the transition line between jetting and dripping in terms of two adimensional parameters: the degree of confinement of the unperturbed jet and a capillary number comparing viscous and interfacial forces. In contrast to a majority of the previous studies [18,19,37], this experimental context naturally leads us to analyze flows confined in microchannels of small cross sections. For pressure-driven flows, this typically results in both strong geometrical confinement and appreciable shear, factors that have been argued to strongly modify the instability of fluid cylinders [38,39]. Given the formidable complexity of the resulting problem, we proceeded with approximations to make progress analytically at low numerical cost. First, we assume that the Reynolds number is small, and we perform a linear analysis using the lubrication approximation (i.e., we formally assume that the perturbation wavelengths

*Corresponding author; annie.colin-exterieur@eu.rhodia.com

are longer than the jet radius). Such a lubrication approach has been shown to successfully capture both qualitative and semiquantative features of the instability in directly related studies of nonconfined cylinders [40,41]. Its validity and application range are analyzed in detail in this section. In the same section we discuss, using concrete examples, the influence on the locus of the transition of both system parameters (surface tension, internal and external viscosities) and operational parameters (inner phase and outer phase flow rates). This allows us in particular to point out and explain a "reentrant" behavior observed in some situations: Increasing progressively the outer phase flow rate can lead first to a transition from jet to drops and then, to a transition back to jet [21].

In Sec. III, we present a method allowing us to extend this approach to microchannels of nonradially symmetric cross sections, a very common situation in microfluidics. This is done at the expense of a further (uncontrolled) approximation, namely we consider only radially symmetric distortions of the unperturbed jet. Then, simple numerical computations of a steady flow in the appropriate geometry allows us to propose quantitative predictions for the droplets-jet transition in various channel geometries (square and rectangle). Sections IV–VI are devoted to the discussion of the results obtained in square and rectangular geometries. Although many features are similar to those obtained for cylindrical channels, significant discrepancies are observed when the flow is strongly confined. This allows us to show that square and rectangle geometries promote the droplets production regime. In contrast, the stability of the jet increases as a function of the confinement. We also point out an unexpected mechanism of droplets production. When the outer phase is less viscous than the inner one and when the jet is large, droplets are formed through a blocking and pinching mechanism. Indeed, in this case, the flow convects the perturbations in the upstream direction. We close the paper with a few remarks, leaving a detailed comparison with experiments to a separate companion paper. A comprehensive calculation of the dispersion equation in the lubrication approximation is reported in the Appendix.

II. LUBRICATION ANALYSIS FOR THE CYLINDRICAL GEOMETRY

We first consider a cylindrically symmetric geometry (see Fig. 1). In a capillary tube of radius R_c two immiscible and incompressible liquids are flowing, an "inner" fluid of viscosity η_i is injected at rate Q_i "in" the stream of "external" liquid of viscosity η_e flowing at rate Q_e.

In the unperturbed state, the flow is unidirectionnal with an inner fluid jet of radius r_i^o and pressure gradients $\partial_z P_e$ and $\partial_z P_i$ in the two fluids that are constants. Together with the boundary conditions at the surface of the jet (continuity of the velocity field and tangential shear stress) and at the walls of the geometry (no slip condition) and local force balance leads to

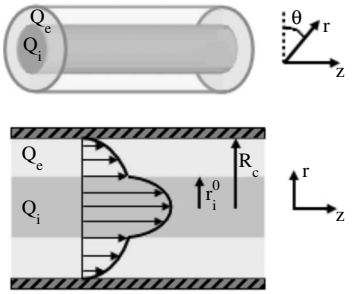

FIG. 1. Flow studied. An internal fluid flows with a flow rate Q_i in an immiscible fluid flowing with a flow rate Q_e. The geometry is a cylindrical capillary tube with a radius R_c. The radius of the inner fluid is r_i^o.

$$Q_e^o = \frac{R_c^2 r_i^{o2}}{4\eta_e}\left[\frac{r_i^{o2}}{R_c^2} - 1 - 2\frac{r_i^{o2}}{R_c^2}\ln\left(\frac{r_i^o}{R_c}\right)\right](\partial_z P_i^o - \partial_z P_e^o) - \frac{\pi(R_c^2 - r_i^{o2})^2}{8\eta_e}\partial_z P_e^o, \tag{1}$$

and

$$Q_i^o = \frac{\pi r_i^{o4}}{2\eta_e}\ln\left(\frac{r_i^o}{R_c}\right)(\partial_z P_i^o - \partial_z P_e^o) - \frac{\pi r_i^{o4}}{8\eta_i}\partial_z P_i^o + \frac{\pi r_i^{o2}(r_i^{o2} - R_c^2)^2}{4\eta_e}\partial_z P_e^o. \tag{2}$$

The two pressure gradients are linked through the continuity of the normal stress at the interface,

$$P_i^o - P_e^o = \frac{\Gamma}{r_i^o}, \tag{3}$$

where Γ is the surface tension. For the unperturbed flow, the radius of the inner jet is constant and the two fluids bear the same pressure gradient.

We perform a linear stability analysis and consider the spatial-temporal response of the system to small z-dependent cylindrically symmetric perturbations δQ_e, δQ_i, $\partial_z \delta P_e$, $\partial_z \delta P_i$, and δr_i. We make the perturbations proportional to $e^{(ikz+\omega t)}$ with k and ω complex numbers. As announced in the introduction, we restrict our analysis to the lubrication approximation, assuming formally that the perturbation wavelength is larger than the radius of the capillary R_c. In this framework, the expressions obtained for the unperturbed flow can still be used locally, so that the local perturbations in the flow rates read as

$$\delta Q_e = \frac{\partial Q_e^o}{\partial(\partial_z P_e^o)}\partial_z \delta P_e + \frac{\partial Q_e^o}{\partial(\partial_z P_i^o)}\partial_z \delta P_i + \frac{\partial Q_e^o}{\partial r_i^o}\partial_z \delta r_i, \tag{4}$$

$$\delta Q_i = \frac{\partial Q_i^o}{\partial(\partial_z P_e^o)}\partial_z \delta P_e + \frac{\partial Q_i^o}{\partial(\partial_z P_i^o)}\partial_z \delta P_i + \frac{\partial Q_i^o}{\partial r_i^o}\partial_z \delta r_i, \tag{5}$$

where the partial derivatives are computed using Eqs. (1) and (2).

However, an important difference is that, as the radius of the jet varies, the Laplace law now requires that the two pressure gradients are different,

$$\partial_z(\delta P_i - \delta P_e) = -\Gamma\left[\partial_z\left(\frac{\delta r_i}{R_c^2} + \partial_z^2 \delta r_i\right)\right], \tag{6}$$

where $\frac{\delta r_i}{R_c^2}$ is proportional to the curvature in the cross section of the jet and $\partial_z^2 \delta r_i$ to the curvature in the flow direction.

This set of equations is equivalent to a computation of the linear response in δr_i, through a second-order expansion in powers of $\epsilon = \frac{R_c}{L_z}$ of the velocity field, where $L_z = \frac{2\pi}{k}$ is the characteristic length scale involved in the z direction. Note that in the lubrication approximation L_z is larger than the capillary radius R_c which implies that $\epsilon \ll 1$. In this expansion, the velocity field reads as

$$v = v_0 + \epsilon v_1 + \epsilon^2 v_2 + O(\epsilon^3). \tag{7}$$

In this framework, an additional approximation is required to obtain Eqs. (4) and (5). In the calculation of the v_2 term, we neglect the pressure gradient created by the term v_0 compared to the one generated by the interface curvature along z. We will quantify more precisely this approximation at the end of this section. A comprehensive computation of these equations is given in the Appendix.

Mass conservation of the incompressible fluids allows us to close the system of equations

$$\delta Q_e + \delta Q_i = 0, \tag{8}$$

$$\partial_t[\pi(r_i^o + \delta r_i)^2] = \partial_z \delta Q_e. \tag{9}$$

We continue with the following set of dimensionless variables:

$$x = \frac{r_i^o}{R_c}, \quad \lambda = \frac{\eta_i}{\eta_e}, \quad \tilde{k} = r_i^o k, \quad \tilde{\omega} = \frac{\omega 16 \eta_e R_c}{\Gamma},$$

$$\widetilde{\delta Q_i} = \frac{8\eta_e}{\pi R_c^4 \partial_z P_i^o}\delta Q_i, \quad \partial_z \widetilde{\delta P_i} = \frac{\partial_z \delta P_i}{\partial_z P_i^o},$$

$$\widetilde{\delta Q_e} = \frac{8\eta_e}{\pi R_c^4 \partial_z P_e^o}\delta Q_e, \quad \text{and } \partial_z \widetilde{\delta P_e} = \frac{\partial_z \delta P_e}{\partial_z P_e^o}. \tag{10}$$

Equations (4) and (5) become Eqs. (11) and (12),

$$\widetilde{\delta Q_e} = a(x)\partial_z \widetilde{\delta P_e} + b(x)\delta x + c(x)(\partial_z \widetilde{\delta P_i} - \partial_z \widetilde{\delta P_e}), \tag{11}$$

$$\widetilde{\delta Q_i} = d(x)\partial_z \widetilde{\delta P_e} + e(x)\delta x + f(x)(\partial_z \widetilde{\delta P_i} - \partial_z \widetilde{\delta P_e}), \tag{12}$$

where

$$a(x) = -(1-x^2)^2, \quad d(x) = 2x^2(x^2-1) - \lambda^{-1}x^4,$$

$$b(x) = 4x(1-x^2), \quad e(x) = 8x^3 - 4\lambda^{-1}x^3 - 4x,$$

$$c(x) = 2x^4 - 2x^2 - 4x^4 \ln(x), \quad f(x) = 4x^4 \ln(x) - \lambda^{-1}x^4.$$

Using Eqs. (6), (8), and (9) we obtain the dispersion equation [Eq. (13)],

$$\tilde{\omega} = \frac{-i\tilde{k}x^3 \,\mathrm{Ka}\, E(x) + F(x)(\tilde{k}^2 - \tilde{k}^4)}{D(x)}, \tag{13}$$

where we have introduced a dimensionless capillary number

$$\mathrm{Ka} = \frac{-\partial_z P^o R_c^2}{\Gamma}$$

and made use of the shorthand notations,

$$E(x,\lambda) = -4x + (8 - 4\lambda^{-1})x^3 + 4(\lambda^{-1} - 1)x^5,$$

$$F(x,\lambda) = x^4[4 - \lambda^{-1} + 4\ln(x)] + x^6(-8 + 4\lambda^{-1}) + x^8[4 - 3\lambda^{-1} - (4 - 4\lambda^{-1})\ln(x)],$$

$$D(x,\lambda) = x^9(1 - \lambda^{-1}) - x^5.$$

$-ix^3\,\mathrm{Ka}\frac{E(x)}{D(x)}\tilde{k}$ summarizes the convection kinematics and the mass conservation, the second term $\frac{F(x)}{D(x)}(\tilde{k}^2 - \tilde{k}^4)$ describes the surface tension effect. E and F are positive functions in cylindrical geometry. Ka is a genuine capillary number as it is the ratio between viscous forces $\eta_e V_e R_c = -\partial_z P^o R_c^3$ and capillary forces ΓR_c. We have however used a notation different from the usual Ca to call the reader's attention to the fact that Ka is a capillary number at the scale of the capillary R_c rather than at the scale of the jet. Obviously in contrast with our approach, studies of unconfined jets focus on capillary numbers defined using either the average jet velocity or the velocity at the surface of the unperturbed jet.

To analyze the stability of the flow, let us create a little bump on the jet and study its evolution. Consider first, the stability of the bump which profile is given by $\delta r_i = \delta r_{io} e^{(ikz+\omega t)}$. The bump will decrease in size, and the flow will be stable if all ω_r are negative. In this study, it is not the case. Indeed, large wavelengths, corresponding to low real values, grow since $F(x)$ is a positive value. Note that the instability comes from the k^2 term which is related to the curvature in the cross section of the jet. Decreasing the size of the jet radius, decreases the interfacial area and energy cost and promotes instability. The term k^4, related to the curvature in the flow direction, is a stabilizing term since undulations in the flow direction increase the interfacial energy cost. With some ω_r positive, an initially localized perturbation generates a growing distortion. A steady state front solution corresponding to a wave vector k^* is selected. The envelope of this front moves with a velocity $v^* = \frac{\omega_r^*}{k_i^*}$. Let us now focus on the stability of this front. If we consider a profile $\delta r_i = \delta r_{io} e^{(ik_o z + \omega t)}$, with ω and k_o complex, it will be unstable against a perturbation with a slightly different wave vector ($k = k_o - i\epsilon$ with ϵ real) when $\mathrm{Re}(\frac{d\omega}{dk} \neq 0)$, since then $e^{\mathrm{Re}(d\omega/dk)\epsilon t}$ always diverges for ϵ values of the same sign as $\frac{d\omega}{dk}$. Hence, front solutions that are stable in the frame moving with the profile must at least satisfy $\frac{\partial \omega_r^*}{\partial k_r} = 0$. If this condition holds, the envelope velocity $\frac{\omega_r^*}{k_i^*}$ where perturbations move with the profile must be equal to the group velocity $\frac{\partial \omega_r^*}{\partial k_i}$ to ensure stability of the front. This leads to the following characteristics for the selected perturbations [8,9,40]:

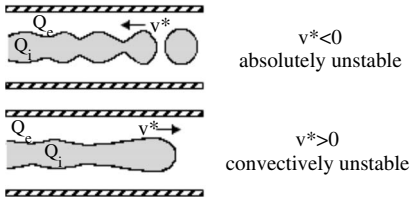

FIG. 2. Schematic representation of the absolute instability and the convective instability. The sytem is absolutely instable when one of v^* is negative and convectively unstable when all the v^* are positive.

$$v^* = \frac{\omega_r^*}{k_i^*}, \quad \frac{\partial \omega_r^*}{\partial k_r} = 0, \quad \text{and} \quad v^* = \frac{\partial \omega_r^*}{\partial k_i}. \tag{14}$$

The system is absolutely unstable if there are solutions such that v^* is negative and convectively unstable if all the solutions v^* are positive. In the former case, a continuous jet can no longer be formed with perturbations propagating backwards. This leads typically to droplets being released intermittently to form a dripping jet, either right at the injection nozzle or at any further point of the entrance zone where the inner stream adjusts its size to the imposed environment. At the opposite, if all v^* are positive, the disturbances which grow in time are simultaneously convected downstream and a continuous jet can persist in the system. Figure 2 gives a schematic representation of the two cases.

Solutions of the dispersion equation that satisfy Eq. (14) lead to four wave vectors that are independent of the imposed flow (or capillary number),

$$\tilde{k}_1^* = + \sqrt{\frac{9+3\sqrt{7}}{24}} + i\sqrt{\frac{-1+\sqrt{7}}{24}},$$

$$\tilde{k}_2^* = - \sqrt{\frac{9+3\sqrt{7}}{24}} + i\sqrt{\frac{-1+\sqrt{7}}{24}},$$

$$\tilde{k}_3^* = + \sqrt{\frac{9+3\sqrt{7}}{24}} - i\sqrt{\frac{-1+\sqrt{7}}{24}},$$

$$\tilde{k}_4^* = - \sqrt{\frac{9+3\sqrt{7}}{24}} - i\sqrt{\frac{-1+\sqrt{7}}{24}}.$$

On the other hand, the corresponding dimensionless real part of the growth rate and the dimensionless front velocity, $\tilde{v}^* = \frac{v^* r_i^o}{\omega_o}$, do depend on the capillary number,

$$\omega_r^* = \frac{\mathrm{Ka}\, E(x) x^3 \tilde{k}_i^* + F(x)\dfrac{5+\sqrt{7}}{18}}{D(x)}. \tag{15}$$

The functions $E(x)$ and $F(x)$ are positive. The wave vectors k_1^* and k_2^* correspond to downstream propagating (and growing) modes with v^* always positive. We thus focus on the disturbances associated to k_3^* and k_4^*, which correspond to the same physics as they differ only by a phase factor. The velocity of the associated perturbations is given by

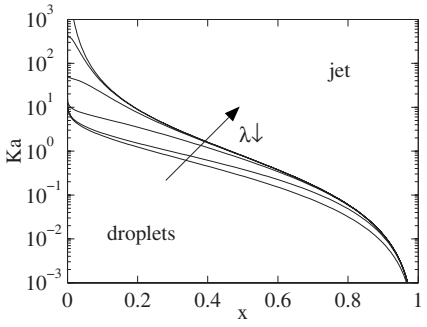

FIG. 3. Phase diagram of the instability in the (x, Ka) plane. The lines correspond to various λ equal from bottom to top to 10, 1, 0.1, 0.01, 0.001, and 0.0001. Above the lines, the jet is convectively unstable, whereas below the lines the jet is absolutely unstable. Regions below the lines correspond to droplets region.

$$\tilde{v}^* = \frac{\mathrm{Ka}\, E(x,\lambda) x^3 - C_1 F(x,\lambda)}{D(x)}, \tag{16}$$

where $C_1 = \frac{5+\sqrt{7}}{18}\sqrt{\left(\frac{24}{\sqrt{7}-1}\right)}$.

For sufficiently low capillary numbers Ka, the corresponding v^* is negative (and $\omega_r^* > 0$), whereas in the opposite limit of high flow speeds and large Ka, v^* becomes positive. This suggests an absolute-to-convective instability transition as the flow rate is increased, with the associated transition from dripping to a continuous jet. We thus reach a rather simple analytical prediction for the transition, $\tilde{v}^*(\mathrm{Ka}, x, \lambda) = 0$, plotted in Fig. 3 in the (x, Ka) plane describing operational conditions for various values of the viscosity ratio system $\lambda = \eta_i / \eta_e$. This plot can be envisioned as a dynamic behavior diagram with a dripping and a jet regime.

For a given λ, increasing the capillary number Ka (i.e., the normalized pressure drop) or the confinement x always eventually lead to a continuous jet. This is physically sound as increasing Ka corresponds to convecting away the perturbations faster, while increasing the confinement x results in slowing down the development rate of the perturbations due to the proximity of the walls. Decreasing $\lambda = \eta_i / \eta_e$ increases the "droplets" regime at the expense of the "jet" regime. The effect of the various systems or operational parameters hidden in the dimensionless variables Ka and x have been studied in detail in [21]. In summary, for fixed flow rates, the droplets formation regime is promoted by high surface tension, large tube diameter, and low internal viscosity. The influence of the external viscosity depends on the situation. More importantly, these studies [21] show the possible occurrence of a qualitatively noticeable effect upon increase of the external flow rate Q_e in an experiment where everything else is fixed. Indeed, raising the value of Q_e can induce a first transition from jetting to dripping and a second one back to jetting. This "reentrant" behavior is qualitatively understood as follows: At low Q_e there is only a thin film of outer phase between the inner jet and the walls, so increasing Q_e essentially reduces the confinement of the jet, which allows the instability to develop faster and thus promotes the formation of droplets. In contrast, at high Q_e when confinement is not significant, increasing Q_e essentially increases the jet veloc-

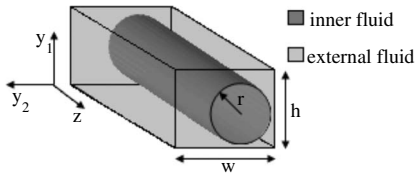

FIG. 4. Notations used for a coflowing jet in a rectangular geometry.

ity, yielding to faster convection downstream of any developing instability, which favors transiting back to a continuous jet.

At this stage, we may comment on the validity of our approximations. Two different approximations have been done. First, we used a dispersion equation derived in the lubrication approximation framework. This implies that the parameter $\epsilon=\frac{r_i^o}{L_z}$ is smaller than 1. The selected wave vector corresponds to a characteristic length in the z direction, L_z, equal to $L_z=2\pi\sqrt{\frac{24}{9+3\sqrt{7}}}r_i^o$. This leads to a value of $\epsilon=\frac{r_i^o}{L_z}=\frac{0.0659}{x}$. Assuming that the use of the dispersion equation obtained in the lubrication approximation framework is valid for $\epsilon<0.2$, we can conclude that this hypothesis is valid for $x>0.33$. Second, we neglected the recirculations inside the perturbated jets. Indeed, in the calculation of the $O(\epsilon^2)$ term, we neglected the pressure gradient created by the term v_0 compared to the one generated by the interface curvature along z. This is valid for $x>0.33$ if $\frac{\eta_i}{\eta_e}<1$ and for $x>0.6$ if $\frac{\eta_i}{\eta_e}>1$. These ranges of parameters correspond thus to the range where our diagrams are fully valid. Note that this point will prevent us to compare quantitatively our results with the ones obtained in unbounded geometries [18,37].

III. EXTENSION OF OUR MODEL TO RECTANGULAR GEOMETRY

In this section, we turn to the most commonly encountered geometry in microfluidics, namely that of a microchannel with a rectangular cross section (see Fig. 4). Two situations must be analyzed. The inner jet may be or not squeezed by the geometric confinement. These two situations correspond, respectively, to $x>1$ and $x<1$, where x is defined as $x=2\sqrt{\frac{s}{\pi h^2}}$, where s is the section of the jet and h is the smallest characteristic size of the rectangular section. If the inner jet is not squeezed by the geometric confinement then, this expression leads to $x=2r/h$, where r is the radius of the jet. We first focus on situations where $x>1$.

A. Squeezed jet in rectangular geometry

We consequently consider as the reference geometry a jet squeezed by the geometry. Moreover, we assume that the outer phase completely wets the walls. In the unperturbated state, the free fluid-fluid interface has a shape involving a single radius curvature (see Fig. 5).

This is a direct consequence of the unidirectional flow. Indeed, the pressure must be constant in each fluid in a channel cross section to avoid the existence of a velocity component in the cross section [30,33]. Reminding that the pressure and the curvature radius are linked through the Laplace equation, we thus get that the curvature radius is constant in a cross section since the pressure is constant in each fluid. The value of the curvature radius is set by wettability conditions and is equal to $h/2$ when the outer phase completely wets the wall. We wish to analyze again the stability of such a jet to axial perturbations without having to move to three-dimensional (3D) numerical simulations. We therefore proceed with an uncontrolled approximation and consider only axially symmetric perturbations of the radius of the jet independent of the polar angle. In the small perturbations case and for $x>1$, the perturbated jet remains squeezed by the geometric confinement. This point is very important, since it sets the shape of the perturbations. Indeed, it ensures that the curvature radius remains constant and equal to $h/2$ in the geometry cross section. The first term in the Laplace equation $(\Gamma\partial_z\delta r_i)$ is thus nil. As a consequence the dispersion equation in the approximation of the lubrication reads as

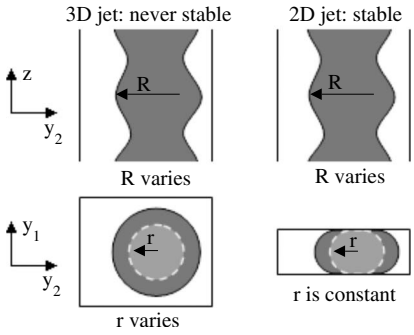

FIG. 5. Schematic representation of a nonsqueezed and a squeezed jet.

$$\tilde{\omega}=\frac{-i\tilde{k}x^3\,\mathrm{Ka}\,E(x)-F(x)(\tilde{k}^4)}{D(x)}. \tag{17}$$

All ω_r are negative and the two-dimensional (2D) jet is thus stable. Confining the jet and squeezing it ensures thus its stability. Perturbations leading to the interfacial area reduction are unable to develop. The same results have been previously derived by Miguel *et al.* [42]. Note also that this scenario of stable 2D jet where the area reduction is killed by the confinement had been experimentally shown by Dollet *et al.* [43] in a flow focusing design. This results explains why coflow situations are often encountered in microfluidic devices [25,30].

B. Nonsqueezed jet in rectangular geometry

We now deal with situations where $x<1$, i.e., where the outer phase completely wets the walls and where the inner jet is not squeezed by the geometric confinement. We consequently consider as the reference geometry a jet completely wrapped by the external phase flowing along z (see Fig. 4 for all notations).

As previously, we analyze again the stability of such a jet to axially symetric perturbations, $r(z)\sim e^{(ikz+\omega t)}$, independent of the polar angle. Although this is certainly not the exact

base of eigenfunctions given the rectangular geometry of the channel, this procedure allows us to proceed rather simply along lines similar to our analysis of the cylindrical case.

We can still write Eqs. (6), (8), (9), (11), and (12), but we need to compute the coefficients $a(x)$, $b(x)$, $c(x)$, $d(x)$, $e(x)$, and $f(x)$ for the geometry of interest.

However, to get those it is sufficient to compute the flow rates *at steady state* in the geometry of Fig. 4 as a function of the jet radius value r and of the pressure gradients in the two phases. The corresponding computation of the flow profile is rather easy as the flow is unidirectional, so that the problem boils down to solving a second-order differential equation in two dimensions [in the (y_1, y_2) plane], which can be numerically achieved in a great variety of geometries. Once these functions are obtained, and thus $E(x)$ and $F(x)$, following exactly the same strategy as in the cylinder case leads to a "phase diagram" for each geometry that can be plotted in a (confinement, capillary number) plane.

The remainder of the paper is organized as follows. First, we present details regarding the numerical procedure we use to compute the functions $a(x)-f(x)$, which the uninterested reader might want to skip. The following sections are devoted to a discussion of the results obtained in three experimentally relevant geometries: A centered jet in a square channel, a centered jet in a rectangular channel, and an off-centered jet in a rectangular channel.

C. Numerical computation scheme

(a) *Equations for the flow field*. At low Reynolds numbers in the unperturbed state, the flow is unidirectional. Conservation of momentum for these incompressible fluids implies that the pressure gradients $\partial_z P_e$, $\partial_z P_i$ are constant. The flow $u(y_1, y_2)$ thus satisfies in each of the two domains (inner and external $\alpha = i, e$),

$$\eta_\alpha \Delta u_\alpha = \partial_z P_\alpha. \tag{18}$$

This set of equations is complemented by appropriate boundary conditions: The velocity and the tangential component of the stress tensor are taken continuous at the interface (jet boundary),

$$u_i = u_e \quad \text{and} \quad \eta_i \frac{\partial u_i}{\partial n} = \eta_e \frac{\partial u_e}{\partial n}, \tag{19}$$

and no slip is required on the walls, $u_e = 0$ [44,45]. Once this set of equations is solved for given values of fluids viscosities, pressure gradients, and jet radius, the flow rates Q_e and Q_i are obtained by performing integrals [33]. (See Fig. 6.)

(b) *Numerical procedure*. The procedure that we actually implement numerically corresponds to solving on a regular Cartesian mesh the equation

$$\nabla \cdot (\eta \nabla u) = \partial_z P, \tag{20}$$

where the functions η and $\partial_z P$ have different values η_α and $\partial_z P_\alpha$ in each of the two internal and external subdomains (again $\alpha = i$ corresponds to the inner phase constituting the jet, while $\alpha = e$ is the external phase wetting the walls). We use a finite volume discretization of the equations that ensures the continuity of the fluxes at the interface [46]. The

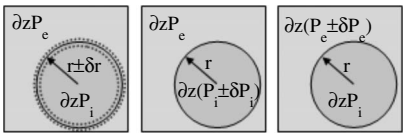

FIG. 6. Parameters variations made in the numerical simulations. Each parameter (r, P_e, and P_i) is slightly varied by keeping the other constant. Both flow rates (Q_i and Q_e) are numerically calculated in each situation. This allows calculating the partial derivative of the flow rates with r, P_e, and P_i.

computations are performed using the scientific software Scilab developed by INRIA.

This allows us to obtain numerically for a given geometry and given fluid viscosities the flow rates $Q_\alpha(\partial_z P_i, \partial_z P_e, x)$, as functions of the pressure gradients in the two phases and of the adimensional "confinement" parameter $x = 2r/h$ that measures the jet radius.

(c) *Calculation of the coefficients*. The functions $a(x)-f(x)$ are then essentially obtained as numerical derivatives of the above functions. For example, $c(x)$ corresponds to the partial derivative of the external flow rate Q_e with respect to the internal pressure gradient $\partial_z P_i$. To compute it, we first compute as described above the flow rates in both fluids for a given *common* pressure gradient $\partial_z P^0 = 1$ and a given shape of the jet x. We then slightly increase (or decrease) the pressure gradient in the internal phase while keeping the pressure gradient in the external phase constant. We compute anew the flow rates in these two slightly modified situations, $Q_e(\partial_z P_i = 1+\delta, \partial_z P_e = 1, x)$ and $Q_e(\partial_z P_i = 1-\delta, \partial_z P_e = 1, x)$. $c(x)$ is then simply given by $c(x) = \frac{Q_e(\partial_z P_i = 1+\delta) - Q_e(\partial_z P_i = 1-\delta)}{2\delta}$. The same or equivalent procedures are used to compute $a(x)$, $d(x)$, and $f(x)$. $e(x)$ and $b(x)$ correspond to partial derivatives with respect to the jet thickness x. We again start with the solution for a common given pressure gradient $\partial_z P^0 = 1$ and a value of x. We then increase or decrease slightly x and, keeping the pressure gradient constant, compute $Q_\alpha(1, 1, x+\delta x)$ and $Q_\alpha(1, 1, x-\delta x)$. Then we have simply $e(x) = \frac{Q_i(x+\delta x) - Q_i(x-\delta x)}{2\delta x}$ and $b(x) = \frac{Q_e(x+\delta x) - Q_e(x-\delta x)}{2\delta x}$.

IV. RESULTS IN A SQUARE GEOMETRY: CENTERED JET

We start with the case of a jet at the center of a square cross-section capillary (dimensions $h \times h$). Results are presented in Fig. 7 in the (x, Ka) plane, with Ka defined as $\mathrm{Ka} = \frac{-\partial_z P^o (h/2)^2}{\Gamma}$, again a capillary number at the scale of the capillary rather than that of the jet. $x > 1$ corresponds to stable bidimensional jet.

We restrict the stability analysis of untruncated jet to variations of x between 0.04 and 0.98, because the computation time becomes very expensive for values closer to 0 and 1 as the computation mesh must be refined. Thus, we do not focus on jets almost contacting the walls.

Results are presented for three viscosity ratios (0.01, 1, and 100), together with the results obtained in the cylindrical geometry for the same values. The global trends and even the numerical values are similar with the exception of the regime

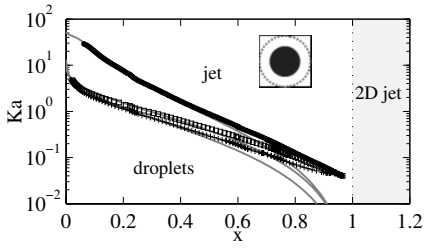

FIG. 7. Phase diagram of the instability in the (x, Ka) plane in a square geometry. The symbols correspond to various viscosity ratios λ. + correspond to λ=100, □ correspond to λ=1, and ● correspond to λ=0.01. Above the symbols the jet is convectively unstable, whereas below the symbols the jet is absolutely unstable. Regions below the symbols correspond to droplets region. $x>1$ correspond to jet absolutely stable. The gray lines correspond to the transition lines obtained in cylindrical geometry. From top to bottom λ=100, λ=1, and λ=0.01.

where x becomes close to 1. In this regime our data suggest that, in contrast to the cylindrical geometry, Ka does not go to 0 as x goes to 1, but tends to a value of order 5×10^{-2}, essentially independent of λ. This increases the range of droplets production and limits the jet stability. A qualitative explanation may be that the presence of the corners allow the instabilities to develop at a finite rate even when $x\to1$ as the outer liquid can be transferred through these corners from regions where the jet is thicker to regions where it is thinner. This suggests a finite threshold for the convective velocity corresponding to roughly the wavelength multiplied by this rate. However, we obviously reach here a regime where our approximation is not accurate: The perturbations are expected to be very noncircular, so that the numbers obtained numerically may be rather inaccurate, although we believe that the trend is definitely correct. Note also, that the values of λ do not change the global behavior of the flow. They affect only the value of the capillary number and of the degree of confinement where the transition between jets and droplets occurs.

Figure 8 presents the transition lines this time plotted against the operational parameters Q_e and Q_i (for realistic values of the parameters in a microfluidic context). The results are remarkably similar to the behavior obtained in cylindrical geometry, in particular for low values of Q_i/Q_e, i.e., at low values of x, as one can expect from Fig. 7. Note again that the lubrication approximation is not very accurate for this degree of confinement. Deviations appear in the opposite limit (note the logarithm scale for Q_e) at higher values of Q_i/Q_e, where droplets are favored over jet in the square geometry. The reentrant scenario of jet→droplets→jet upon increase of Q_e obviously persists in this geometry. However, two different jets are observed at low Q_e. At very low value of Q_e, the jet is absolutely stable. It is squeezed by the geometry and touches the walls. Increasing Q_e at fixed Q_i decreases the size of the jet until it does not reach the walls anymore. At this stage, the jet is convectively stable. Then the situation becomes similar to the one previously described in cylindrical geometry and a reentrant behavior is observed for the same causes.

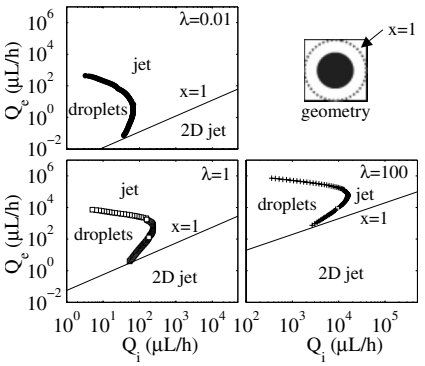

FIG. 8. Flow rate at the transitions between absolute and convective instability in a 100 μm high square channel for various viscosity ratios. The viscosity of the inner phase is set at 0.1 Pa s. + correspond to λ=100, □ correspond to λ=1, and ● correspond to λ=0.01. Above the symbols the jet is convectively unstable, whereas below the symbols the jet is absolutely unstable. The region below the symbols corresponds to droplets regime. Lines correspond to flow rates for which the jet touches the walls. Below these lines, the jets are absolutely stable (2D jets).

V. RESULTS IN A RECTANGULAR GEOMETRY: CENTERED JET

We now turn to channels with rectangular cross sections and perform explicit computations for the case $w=2h$. This leads to Fig. 9, where again, the (vertical) confinement is measured by $x=2\sqrt{\frac{s}{\pi h^2}}$ which is equivalent to $x=2r/h$ for $x<1$. Ka is a capillary number involving the channel thickness, $\mathrm{Ka}=\frac{-\partial_z P^o (h/2)^2}{\Gamma}$.

As previously, $x>1$ corresponds to a stable bidimensional jet. This behavior does not depend upon λ. We scan values of x between 0.04 and 0.98. For λ<1, the trend is similar to the one found for square cross section, with a dripping regime even more increased at high values of x which means that higher values of Ka are required to obtain continuous jets. In the limit of $x\to1$ the critical Ka is about 4 times larger. This trend is expected from our previous discussion of the square case: Here the absence of confinement

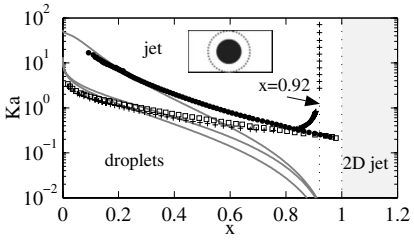

FIG. 9. Phase diagram of the instability in the (x, Ka) plane in a rectangular geometry with an aspect ratio of 2. The symbols correspond to various λ. + correspond to λ=100, □ correspond to λ=1, and ● correspond to λ=0.01. Above the symbols the jet is convectively unstable, whereas below the symbols the jet is absolutely unstable. The region below the symbols corresponds to droplets regime. The gray lines correspond to the transition lines obtained in a cylindrical geometry. From top to bottom λ=100, λ=1, and λ=0.01.

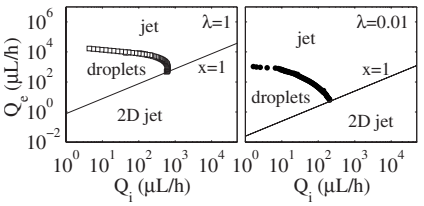

FIG. 10. Flow rate at the transitions between absolute and convective instability in a 100 μm high and 200 μm wide rectangular channel for various viscosity ratios. The viscosity of the inner phase is set at 0.1 Pa s. □ correspond to $\lambda=1$ and ● correspond to $\lambda=0.01$. Above the symbols the jet is convectively unstable, whereas below the symbols the jet is absolutely unstable. Regions below the symbols correspond to droplets region. Below the line the jet is a 2D jet absolutely stable.

in the horizontal direction makes it even easier for perturbations to develop faster. For $\lambda>1$, a different behavior appears in the vicinity of $x=0.92$. The curve $\mathrm{Ka}=f(x)$ increases as a function of x and goes to infinity when x goes to 0.92. The flow in the zone $x\in[0.92,1]$ is absolutely unstable. At first sight, this behavior seems not to be physically sound. One may expect that increasing the size of the jet and thus increasing the confinement will promote the stability of the flow. Analyzing in more details our computation, we note that the sign of the function $E(x)$ changes and becomes negative for $x>0.92$. As noticed previously, the term $E(x)$ summarizes the kinematics of convection and mass conservation in the dispersion equation. Intuitively, one would expect this term to be always of the same sign, i.e., positive: Perturbations are convected downstream. The negative values of $E(x)$ in this rectangular geometry for $x\in[0.92,1]$, imply that the flow convects the growing perturbations upstream. We thus point out here a new mechanism of droplets formation. Droplets are formed not because the shear forces are weaker than the capillary ones, but because the flow convects the growing front upstream. Note that this particular behavior occurs only for $\lambda=\frac{\eta_i}{\eta_e}>1$.

Figure 10 presents phase diagrams in the (Q_i,Q_e) plane for $\lambda<1$. The results are similar to the behavior obtained in cylindrical or square geometries, in particular for low Q_i/Q_e values, i.e., at low x values. As in the cylindrical and square geometries, a reentrant behavior is evidenced. However, its nature varies. Bidimensional jets, droplets, and thin jets are observed when x is increased for a fixed low Q_i. Large stable jets stabilized by the vicinity of the walls are absent from this diagram.

Figure 11 presents phase diagrams in the (Q_i,Q_e) plane for explicit geometries for $\lambda>1$. This diagram is much more complex than the one obtained for $\lambda<1$. First, as noticed above, it evidences a new flow pattern. Droplets are obtained for a large value of the internal flow rate and are produced due to the upstream propagation of the perturbations. This corresponds to a blocking and pinching mechanism. In the following, this flow pattern will be noted $v^*>0$. Second, this diagram evidences areas where different states may exist or coexist for the same values of Q_i and Q_e. Let us comment on this last point. For $\lambda>1$, the curve $\frac{Q_i}{Q_e}$ (see top graph of Fig. 11) as a function of x displays a local maximum for x

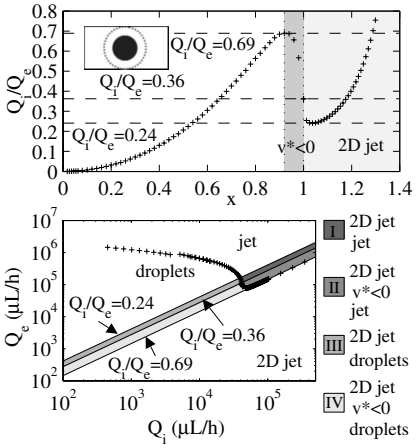

FIG. 11. Top graph: Q_i/Q_e as a function of x for $\lambda=100$ in a 100 μm high and 200 μm wide rectangular channel. The viscosity of the inner phase is set at 0.1 Pa s. The curve is multivalued. Three different values of x correspond to the same flow rate ratio. The curve presents a decreasing branch for $x\in[0.92,1.037]$. Bottom graph: Flow rate at the transitions between absolute and convective instability for the same experimental conditions. Grat regions correspond to area where different states may exist or coexist. Region I corresponds to 2D jets or to convected jet, region II to 2D jets, convected jet or blocking pinching droplets, region III to 2D jets or droplets, region IV to 2D jets, droplets and blocking pinching droplets. Below the line, the jet is a 2D jet absolutely stable. Above the symbols, the jet is convectively stable.

$=0.92$ and a local minimum for $x=1.037$ (see Fig. 11). For $\frac{Q_i}{Q_e}$ ranging between 0.24 and 0.69, three differents values of x may coexist for the same value of $\frac{Q_i}{Q_e}$. This implies that different situations must be analyzed in this (Q_i,Q_e) zone and that different states may exist or coexist in this range of flow rates. Let us now discuss in more details the bottom graph of Fig. 11. The region $\frac{Q_i}{Q_e}>0.69$ corresponds to bidimensional stable jets. These flows are stable. The region $0.24<\frac{Q_i}{Q_e}<0.36$ and the region $0.36<\frac{Q_i}{Q_e}<0.69$ are areas where setting a value to Q_i, and another one to Q_e does not allow us to select a unique x and thus where different situations might be encountered at a single point in the (Q_i,Q_e) plane.

For $0.36<\frac{Q_i}{Q_e}<0.69$, 2D jets, droplets or blocking pinching droplets with $v^*<0$ are encountered for low values of Q_i (region IV), where as 2D jets, jets stabilized by the velocity or blocking pinching droplets with $v^*<0$ are evidenced for high values of Q_i (region II).

For $0.24<\frac{Q_i}{Q_e}<0.36$, 2D jets and droplets occur for low values of Q_i (region III) whereas 2D jets and jets stabilized by the velocity are encountered for high values of Q_i (region I).

The region $\frac{Q_i}{Q_e}<0.24$ looks like the one obtained for $\lambda<1$. Droplets are obtained for low values of Q_i and jets stabilized by the velocity are observed for high values of Q_i.

Note that at this stage, we are unable to predict the flow and its stability of the flow in the gray zone. Indeed, we do not know what are the parameters that will select the nature of the flow and discriminate, for exemple, between a 2D jet

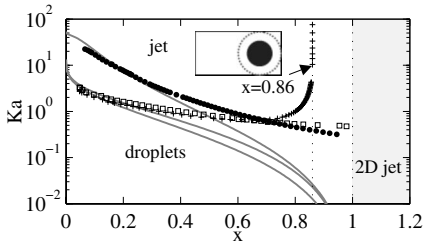

FIG. 12. Phase diagram of the instability in the (x, Ka) plane in a rectangular geometry with a aspect ratio of 2. The jet is not centered. The symbols correspond to various λ. + correspond to λ =100, □ correspond to λ=1, and ● correspond to λ=0.01. Above the symbols the jet is convectively unstable, whereas below the symbols the jet is absolutely unstable. Regions below the symbols correspond to droplets region. The gray lines correspond to the transition lines obtained in a cylindrical geometry. From top to bottom λ=100, λ=1, and λ=0.01.

or droplets. We believe that hysteritical behavior might be evidenced and that different states will be encountered by increasing or decreasing the flow rate ratio. Experiments are clearly required to probe these mechanisms.

VI. RESULTS IN A RECTANGULAR GEOMETRY: THE DECENTERED JET

We now turn to an even less symmetrical situation, corresponding to an off-centered jet in the same rectangular channel as in the preceding subsection. The geometry is presented in Fig. 12. The jet is still vertically centered, but is horizontally shifted so that its center is at $h/2$ from the vertical wall. In this geometry, we still use the parameter $x=2\sqrt{\frac{s}{\pi h^2}}$ to describe the confinement and because of our flow geometry it goes to 1 when the jet simultaneously approaches the top, bottom, and lateral wall.

As previously, $x>1$ corresponds to a stable bidimensional jet and this behavior does not depend upon λ. For the plot in Fig. 12, x is varied between 0.04 and 0.98. Again the general trends in the (x, Ka) plane are the same, i.e., decrease of the critical Ka with confinement. The same behaviour due to the same causes is observed for λ>1. The curve Ka=$f(x)$ goes to infinity when x goes to 0.86. The flow in the zone $x \in [0.86, 1]$ is absolutely unstable. As previously, this zone corresponds to flows where perturbations are convected upstream.

Figure 13 displays the obtained results in the (Q_i, Q_e) plane for for λ<1. The behavior is exactly the same as the one observed for the centered jet. We note however that the droplets production area is smaller. This is not surprising since one expects this geometry (essentially three confining walls) to yield intermediate results between the square (four confining walls) and the centered rectangle (two confining walls). Figure 14 displays the obtained results in the (Q_i, Q_e) plane for for λ>1. The behavior is exactly the same as the one observed for the centered jet. We note however that the region where different states may exist for a single value of the couple (Q_i, Q_e) is larger in this geometry.

VII. CONCLUSION

In this work, using the lubrication approximation and focusing on low Reynolds numbers, we have studied the stability of a pressure-driven jet confined in a capillary. Analyzing the transition from a continuous jet to a dripping system in terms of a convective-absolute transition, we find the jet to remain continuous at high capillary numbers and to break down into droplets at lower flow rates, i.e., pressure gradients. Analytical formulas are provided in cylindrical capillaries for a given system where viscosities and surface tension are known. The influence of the various system and operation parameters have been highlighted. At the expense of further approximations, we have explored other microchannel geometries, that are more relevant in the microfluidics context given fabrication processes. Microchannels of square or rectangular cross section promote droplets at strong confinement when contrasted with their cylindrical counterparts, most likely because corners allow easier fluid transfer. We

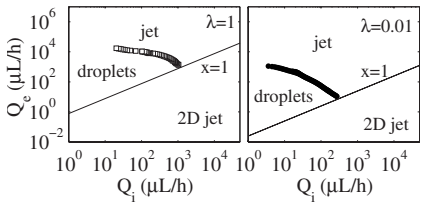

FIG. 13. Flow rate at the transitions between absolute and convective instability in a 100 μm high and 200 μm wide rectangular channel for various viscosity ratios. The viscosity of the inner phase is set at 0.1 Pa s. □ correspond to λ=1 and ● correspond to λ =00.1. Above the symbols the jet is convectively unstable, whereas below the symbols the jet is absolutely unstable. Regions below the symbols correspond to droplets region.

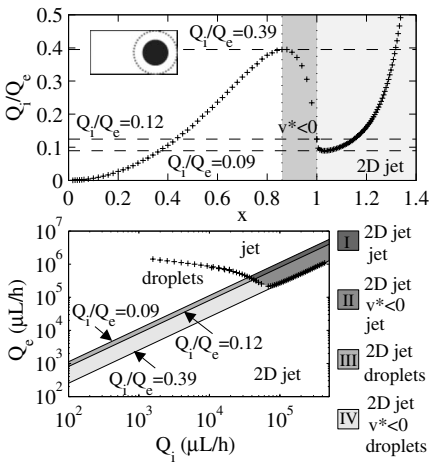

FIG. 14. Top graph: Q_i/Q_e as a function of x for λ=100 in a 100 μm high and 200 μm wide rectangular channel for a decentered jet. The viscosity of the inner phase is set at 0.1 Pa s. The curve is multivalued. Three different values of x correspond to the same flow rate ratio. The curve presents a decreasing branch for $x \in [0.92, 1.031]$. Bottom graph: Flow rate at the transitions between absolute and convective instability for the same experimental conditions. Gray regions correspond to area where different states may exist or coexist. Region I corresponds to 2D jets or to convected jet, region II to 2D jets, convected jet or blocking pinching droplets, region III to 2D jets or droplets, region IV to 2D jets, droplets, and blocking pinching droplets. Below the line, the jet is a 2D jet absolutely stable. Above the symbols, the jet is convectively stable.

have provided numerical plots on the locus of the transition for rectangles of aspect ratio 1 (squares) and 2. In all the examined geometries, we predict a reentrant jet→droplets →jet evolution as the flow rate of the external phase is increased. We have evidenced very particular behavior for $\lambda < 1$, i.e., when a viscous internal fluid is wrapped by a less viscous fluid. Different states seem to exit for a single couple of (Q_i, Q_e). In particular, in this zone we have evidenced a new mechanism of droplet production that involves perturbations flowing upstream. This mechanism seems to correspond to the blocking-pinching mechanism often described in the literature. Experiments are required to probe these points in more details. To validate this approach, we perform in a companion paper a detailed comparison with experimental measurements complementary to the ones presented in [21].

ACKNOWLEDGMENTS

The authors gratefully acknowledge support from Aquitaine Région. They wish to thank Julie Goyon and Mathieu Joanicot for valuable discussions.

APPENDIX

We propose to validate our approach and to show that our approximation in cylindrical geometry is equivalent to a computation of the linear response in δr_i, through a second-order expansion in powers of $\epsilon = \frac{R_c}{L_z}$ of the velocity field with a supplementary approximation. We recall that L_z is the characteristic lengh scale in the z direction involved in the perturbation. In the perturbed state, the inner fluid jet radius varies as $r_i^o + \delta r_i e^{(ikz+\omega t)}$. The velocity field $\mathbf{v}$ remains axisymetric but is not anymore unidirectional. It reads $\mathbf{v} = v_r^\alpha \mathbf{e_r} + v_z^\alpha \mathbf{e_z}$ where $\alpha = i$ refers to the internal fluid and $\alpha = e$ to the external one. We introduce the following set of dimensionless variables:

$$\bar{r} = \frac{r}{R_c}, \quad x = \frac{r_i^o}{R_c}, \quad \epsilon = \frac{R_c}{L_z}, \quad \bar{z} = \frac{z}{L_z},$$

$$\lambda = \frac{\eta_i}{\eta_e}, \quad \bar{k} = L_z k, \quad \bar{t} = \frac{t}{T}, \quad \bar{\omega} = \omega T,$$

$$\overline{v_r^\alpha} = \frac{v_r^\alpha}{v_{ro}}, \quad \bar{p} = \frac{p}{\Delta p_o}, \quad \delta x = \frac{\delta r_i}{R_c}, \quad \overline{v_z^\alpha} = \frac{v_z^\alpha}{v_{zo}},$$

$$A = \frac{v_{zo} L_z \eta_i}{\Delta p_o R_c^2}, \quad B = \frac{\Gamma}{R_c \Delta p_o}, \quad C_i = 1, \quad C_e = \lambda^{-1}, \quad \text{(A1)}$$

where Δp_o is the pressure drop between the microchannel inlet and outlet in the nonperturbed case. The various scales are linked through the following equations:

$$\frac{R_c}{T v_{ro}} = 1, \quad v_{ro} = \epsilon v_{zo}, \quad \text{and} \quad \frac{T v_{zo}}{L_z} = 4. \quad \text{(A2)}$$

We write the mass conservation and the Stokes equation for both fluids and obtain

$$0 = \frac{\delta \overline{v_z^\alpha}}{\delta \bar{z}} + \frac{\delta \overline{v_r^\alpha}}{\delta \bar{r}} + \frac{\overline{v_r^\alpha}}{\bar{r}},$$

$$\frac{\delta \overline{p^\alpha}}{\delta \bar{z}} = C_\alpha A \left(\frac{\delta^2 \overline{v_z^\alpha}}{\delta^2 \bar{r}} + \frac{1}{\bar{r}} \frac{\delta \overline{v_z^\alpha}}{\delta \bar{r}} + \epsilon^2 \frac{\delta^2 \overline{v_z^\alpha}}{\delta^2 \bar{r}} \right),$$

$$\frac{\delta \overline{p^\alpha}}{\delta \bar{r}} = C_\alpha A \epsilon^2 \left(\frac{\delta^2 \overline{v_r^\alpha}}{\delta^2 \bar{r}} + \frac{1}{\bar{r}} \frac{\delta \overline{v_r^\alpha}}{\delta \bar{r}} + \epsilon^2 \frac{\delta^2 \overline{v_r^\alpha}}{\delta^2 \bar{r}} \right). \quad \text{(A3)}$$

The no-slip condition at the wall and the continuity of the velocity field at the interface read as

$$\overline{v_z^e} = \overline{v_r^e} = 0 \quad \text{for } \bar{r} = 1,$$

$$\overline{v_z^i} = \overline{v_z^e} \quad \text{for } \bar{r} = x + \delta x e^{i\bar{k}\bar{z} + \bar{\omega}\bar{t}},$$

$$\overline{v_r^i} = \overline{v_r^e} \quad \text{for } \bar{r} = x + \delta x e^{i\bar{k}\bar{z} + \bar{\omega}\bar{t}}. \quad \text{(A4)}$$

By definition of the velocity, we moreover obtain a link between the jet radius $r_i^o + \delta r_i e^{(i\bar{k}\bar{z} + \bar{\omega}\bar{t})}$ and the radial component of the velocity. We recall that $\frac{D\bar{r}}{Dt} = \mathbf{v} \cdot \mathbf{e_r}$. In dimensionless form, it reads as

$$\overline{v_r^i} = + i\bar{k} \overline{v_z^i} + \frac{\delta \delta x}{\delta \bar{t}}. \quad \text{(A5)}$$

In the framework of the the linear response in δx, the continuity of the stress at the interface for $\bar{r} = x + \delta x e^{i\bar{k}\bar{z} + \bar{\omega}\bar{t}}$ reads as

$$\sigma_{zr}^i + \epsilon \delta x e^{i\bar{k}\bar{z} + \bar{\omega}\bar{t}} (\sigma_{rr}^i - \sigma_{zz}^i) = \sigma_{zr}^e + \epsilon \delta x e^{i\bar{k}\bar{z} + \bar{\omega}\bar{t}} (\sigma_{rr}^e - \sigma_{zz}^e), \quad \text{(A6)}$$

$$\sigma_{rr}^i - \sigma_{rr}^e - 2i\bar{k}\epsilon \delta x e^{(i\bar{k}\bar{z} + \bar{\omega}\bar{t})} (\sigma_{rz}^i - \sigma_{rz}^e) = \frac{\Gamma}{R_c p_o} \left(\frac{1}{x} - \frac{\delta x e^{i\bar{k}\bar{z} + \bar{\omega}\bar{t}}}{x^2} + \epsilon^2 \bar{k}^2 \delta x e^{i\bar{k}\bar{z} + \bar{\omega}\bar{t}} \right). \quad \text{(A7)}$$

We develop the pressure and the velocity field in power of ϵ and we solve the previous set of equations in the framework of the linear response in δx,

$$\overline{p^\alpha} = \overline{p_0^\alpha} + \epsilon \overline{p_1^\alpha} + \epsilon^2 \overline{p_2^\alpha},$$

$$\overline{v_z^\alpha} = \overline{v_{0z}^\alpha} + \epsilon \overline{v_{1z}^\alpha} + \epsilon^2 \overline{v_{2z}^\alpha},$$

$$\overline{v_r^\alpha} = \overline{v_{0r}^\alpha} + \epsilon \overline{v_{1r}^\alpha} + \epsilon^2 \overline{v_{2r}^\alpha}. \quad \text{(A8)}$$

At the zeroth order in ϵ and in the framework of the linear response in δx, Eq. (A3) becomes

$$0 = \frac{\delta \overline{v_{0z}^\alpha}}{\delta \bar{z}} + \frac{\delta \bar{r} \overline{v_{0r}^\alpha}}{\delta \bar{r}},$$

$$\frac{\delta \overline{p_0^\alpha}}{\delta \bar{z}} = C_\alpha A \left(\frac{\delta^2 \overline{v_{0z}^\alpha}}{\delta^2 \bar{r}} + \frac{1}{\bar{r}} \frac{\delta \overline{v_{0z}^\alpha}}{\delta \bar{r}} \right),$$

$$\frac{\delta\overline{p_0^\alpha}}{\delta\bar{r}} = 0. \tag{A9}$$

This leads to the following velocity and pressure fields:

$$\overline{v_{0z}^i} = a^i(\bar{z})\frac{\bar{r}^2}{4} + c^i(\bar{z}),$$

$$\overline{v_{0z}^e} = a^e(\bar{z})\left(\frac{\bar{r}^2}{4} - \frac{1}{4}\right) + b^e(\bar{z}),$$

$$\overline{v_{0r}^i} = -\frac{\delta a^i(\bar{z})}{\delta\bar{z}}\frac{\bar{r}^3}{16} - \frac{\delta c^i(\bar{z})}{\delta z}\frac{\bar{r}}{2},$$

$$\overline{v_{0r}^e} = -\frac{\delta a^e(\bar{z})}{\delta\bar{z}}\left(\frac{\bar{r}^3}{16} - \frac{\bar{r}}{8} - \frac{1}{\bar{r}}\right) - \frac{\delta b^e(\bar{z})}{\delta\bar{z}}\left(\frac{\bar{r}\ln\bar{r}}{2} - \frac{\bar{r}}{2} + \frac{1}{2\bar{r}}\right),$$

$$\Delta\overline{p_0^i} = \bar{z} + \frac{B}{x} + \delta\overline{p_0^i}e^{i\bar{k}\bar{z}+\omega t},$$

$$\Delta\overline{p_0^e} = \bar{z} + \delta\overline{p_0^e}e^{i\bar{k}\bar{z}+\omega t},$$

$$\delta\overline{p_0^i} = \delta\overline{p_0^e} - \frac{B\delta x}{x^2}, \tag{A10}$$

with

$$a^i(\bar{z}) = (1 + ik\delta\overline{p_0^i}e^{i\bar{k}\bar{z}+\bar{\omega}\bar{t}})/AC_i,$$

$$a^e(\bar{z}) = (1 + ik\delta\overline{p_0^e}e^{i\bar{k}\bar{z}+\bar{\omega}\bar{t}})/AC_e,$$

$$b^e(\bar{z}) = \frac{B\delta x i\bar{k}e^{i\bar{k}\bar{z}+\bar{\omega}\bar{t}}}{2AC_e},$$

$$c^i(\bar{z}) = a^e(\bar{z})\frac{x^2-1}{4} + b^e(\bar{z})\ln x - a^i(\bar{z})\frac{x^2}{4}. \tag{A11}$$

The calculation at the first order in ϵ is straigthforward and gives $\overline{p_1^\alpha}=\overline{v_{1z}^\alpha}=\overline{v_{1r}^\alpha}=0$. At the second order in ϵ, we must solve

$$0 = \frac{\delta\overline{v_{2z}^\alpha}}{\delta\bar{z}} + \frac{\delta\overline{v_{2r}^\alpha}}{\delta\bar{r}} + \frac{\overline{v_{2r}^\alpha}}{\bar{r}},$$

$$\frac{\delta\overline{p_2^\alpha}}{\delta\bar{z}} = C_\alpha A\left(\frac{\delta^2\overline{v_{2z}^\alpha}}{\delta^2\bar{r}} + \frac{1}{\bar{r}}\frac{\delta\overline{v_{2z}^\alpha}}{\delta\bar{r}} + \frac{\delta^2\overline{v_{0z}^\alpha}}{\delta^2\bar{r}}\right),$$

$$\frac{\delta\overline{p_2^\alpha}}{\delta\bar{r}} = C_\alpha A\left(\frac{\delta^2\overline{v_{0r}^\alpha}}{\delta^2\bar{r}} + \frac{1}{\bar{r}}\frac{\delta\overline{v_{0r}^\alpha}}{\delta\bar{r}}\right). \tag{A12}$$

This leads us to

$$0 = \frac{\delta\overline{v_{2z}^\alpha}}{\delta\bar{z}} + \frac{\delta\overline{v_{2r}^\alpha}}{\delta\bar{r}} + \frac{\overline{v_{2r}^\alpha}}{\bar{r}},$$

$$\frac{\delta}{\delta\bar{z}}\int C_\alpha A\left(\frac{\delta^2\overline{v_{0r}^\alpha}}{\delta^2\bar{r}} + \frac{1}{\bar{r}}\frac{\delta\overline{v_{0r}^\alpha}}{\delta\bar{r}}\right) + ik\delta\overline{p_2^\alpha}e^{i\bar{k}\bar{z}+\bar{\omega}\bar{t}} = C_\alpha A\left(\frac{\delta^2\overline{v_{2z}^\alpha}}{\delta^2\bar{r}} + \frac{1}{\bar{r}}\frac{\delta\overline{v_{2z}^\alpha}}{\delta\bar{r}} + \frac{\delta^2\overline{v_{0z}^\alpha}}{\delta^2\bar{r}}\right). \tag{A13}$$

Moreover, if we neglect $\frac{\delta}{\delta\bar{z}}\int C_\alpha A(\frac{\delta^2\overline{v_{0r}^\alpha}}{\delta^2\bar{r}} + \frac{1}{\bar{r}}\frac{\delta\overline{v_{0r}^\alpha}}{\delta\bar{r}})$ and $C_\alpha A\frac{\delta^2\overline{v_{0z}^\alpha}}{\delta^2\bar{r}}$ in front of $\frac{\delta\overline{p_2^\alpha}}{\delta\bar{z}}$ we obtain

$$0 = \frac{\delta\overline{v_{2z}^\alpha}}{\delta\bar{z}} + \frac{\delta\overline{v_{2r}^\alpha}}{\delta\bar{r}} + \frac{\overline{v_{2r}^\alpha}}{\bar{r}},$$

$$\frac{\delta\overline{p_2^\alpha}}{\delta\bar{z}} = C_\alpha A\left(\frac{\delta^2\overline{v_{2z}^\alpha}}{\delta^2\bar{r}} + \frac{1}{\bar{r}}\frac{\delta\overline{v_{2z}^\alpha}}{\delta\bar{r}}\right), \tag{A14}$$

which is the same set of equations already solved for the zeroth-order equation. The calculation of the velocity field and pressure field leads to

$$\overline{v_{2z}^i} = a_2^i(\bar{z})\frac{\bar{r}^2}{4} + c_2^i(\bar{z}),$$

$$\overline{v_{2z}^e} = a_2^e(\bar{z})\left(\frac{\bar{r}^2}{4} - \frac{1}{4}\right) + b_2^e(\bar{z}) + c_2^e(\bar{z}),$$

$$\overline{v_{2r}^i} = -\frac{\delta a_2^i(\bar{z})}{\delta\bar{z}}\frac{\bar{r}^3}{16} - \frac{\delta c_2^i(\bar{z})}{\delta\bar{z}}\frac{\bar{r}}{2},$$

$$\overline{v_{2r}^e} = -\frac{\delta a^e(\bar{z})}{\delta\bar{z}}\left(\frac{\bar{r}^3}{16} - \frac{\bar{r}}{8} - \frac{1}{\bar{r}}\right) - \frac{\delta b^e(\bar{z})}{\delta\bar{z}}\left(\frac{\bar{r}\ln\bar{r}}{2} - \frac{\bar{r}}{2} + \frac{1}{2\bar{r}}\right),$$

$$\overline{p_2^i} = -\frac{Bx^2\bar{k}^2}{x} + \delta\overline{p_2^i}e^{i\bar{k}\bar{z}+\bar{\omega}\bar{t}},$$

$$\overline{p_2^e} = \delta\overline{p_2^e}e^{i\bar{k}\bar{z}+\bar{\omega}\bar{t}},$$

$$\delta\overline{p_2^i} = \delta\overline{p_2^e} + B\bar{k}^2\delta x, \tag{A15}$$

with

$$a_2^i(\bar{z}) = (ik\delta\overline{p_2^i}e^{i\bar{k}\bar{z}+\bar{\omega}\bar{t}})/AC_e,$$

$$a_2^e(\bar{z}) = (ik\delta\overline{p_2^e}e^{i\bar{k}\bar{z}+\bar{\omega}\bar{t}})/AC_i,$$

$$b_2^e(\bar{z}) = \frac{B\delta x i\bar{k}e^{i\bar{k}\bar{z}+\bar{\omega}\bar{t}}}{2AC_e},$$

$$c_2^i(\bar{z}) = a_2^e(\bar{z})\frac{x^2-1}{4} + b_2^e(\bar{z})\ln x - a_2^i(\bar{z})\frac{x^2}{4}. \tag{A16}$$

Reporting Eqs. (A10) and (A15) in the boundary conditions and Eq. (A5) leads to the dispersion equation

$$\bar{\omega} = \frac{i\bar{k}x}{4AC_e}\frac{E(x,\lambda)}{D(x,\lambda)} + \frac{(\bar{k}^2x^2 - \epsilon^2\bar{k}^4x^4)B}{4AC_e}\frac{F(x,\lambda)}{D(x,\lambda)}. \tag{A17}$$

This equation may be rewritten in terms of the variable used in the text, remembering that

$$\tilde{k} = \epsilon \bar{k} x, \quad \mathrm{Ka} = \frac{\epsilon}{B}, \quad \tilde{\omega} = \frac{\omega 16 \eta_e R_c}{\Gamma}, \quad \text{and} \quad \frac{T v_{zo}}{L_z} = 4. \tag{A18}$$

We then obtain the dispersion equation presented in the first paragraph of the paper,

$$\tilde{\omega} = i\tilde{k}\,\mathrm{Ka}\frac{E(x,\lambda)}{D(x,\lambda)} + (\tilde{k}^2 - \tilde{k}^4)\frac{F(x,\lambda)}{D(x,\lambda)}. \tag{A19}$$

The lubrication approximation used in this work is thus equivalent to a computation of the linear response in δr_i, through a second-order expansion in powers of ϵ of the velocity field with a supplementary approximation. Indeed, we have neglected the dependence on r of the pressure field at the second order in ϵ. From a more physical point of view this means that we have neglected the recirculations induced by the radial velocity. To compute the range of validity of such an approximation, one must compare $\frac{\delta}{\delta z}\int C_\alpha A(\frac{\delta^2 \overline{v_{0r}^\alpha}}{\delta^2 \bar{r}} + \frac{1}{\bar{r}}\frac{\delta \overline{v_{0r}^\alpha}}{\delta \bar{r}})$ and $C_\alpha A \frac{\delta^2 \overline{v_{0z}^\alpha}}{\delta^2 \bar{r}}$ in front of $\frac{\delta \overline{p_2^\alpha}}{\delta \bar{z}}$. Figure 15 reports such a comparison. The pressure gradient involved in the internal recirculations are plotted using dashed lines wheres $\frac{\delta \overline{p_2^\alpha}}{\delta \bar{z}}$ is plotted using a filled line. The comparison is performed for various initial size of the unperturbated jet. This comparison requires the knowledge of various parameters such as $\bar{k}$, B, and A. In the following, we take $\bar{k}=1$ and $A=1$. The value of B is calculated in order to obtain a capillary number Ka close to the one observed at the transition (see Fig. 3). Figures 15(a)–15(c) show that the approximation holds for $x=0.9$ and $x=0.55$ for $\frac{\eta_i}{\eta_e}<1$. However, this approximation is no longer valid if $x<0.55$ and $\frac{\eta_i}{\eta_e}>1$. A comprehensive study leads to the following conclusion. Our approximation holds for $x>0.3$ if $\frac{\eta_i}{\eta_e}<1$ and for $x>0.6$ if $\frac{\eta_i}{\eta_e}>1$ (see Fig. 15).

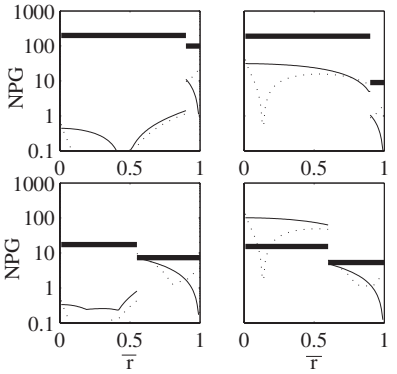

FIG. 15. Comparison between the modulus of the neglected terms and the modulus of the normalized pressure gradient (NPG). The dotted lines correspond to $\frac{\delta}{\delta \bar{z}}\int CA(\frac{\delta^2 \overline{v_{0r}^\alpha}}{\delta^2 \bar{r}} + \frac{1}{\bar{r}}\frac{\delta \overline{v_{0r}^\alpha}}{\delta \bar{r}})$, the lines correspond to $CA\frac{\delta^2 \overline{v_{0z}^\alpha}}{\delta^2 \bar{z}}$, and the large lines correspond to $\bar{k}\delta\overline{p}_2^i$. In (a) $\lambda=0.1$, $x=0.9$, and $B=100$; in (b) $\lambda=0.1$, $x=0.55$, and $B=10$; in (c) $\lambda=50$, $x=0.9$, and $B=100$; and in (d), $\lambda=50$, $x=0.55$, and $B=10$.

[1] J. Plateau, *Statique Expérimentale et Théorique des Liquides Soumis aux Seules Forces Moléculaires* (Gauthier-Villars, Paris, 1873), pp. 450–495.
[2] Lord Rayleigh, Proc. London Math. Soc. **10**, 4 (1879).
[3] Lord Rayleigh, Proc. R. Soc. London **29**, 71 (1879).
[4] S. P. Lin, *Breakup of Liquid Sheets and Jets* (Cambridge University Press, Cambridge, England, 2003).
[5] S. P. Lin and R. D. Reitz, Annu. Rev. Fluid Mech. **30**, 85 (1998).
[6] J. Eggers, Rev. Mod. Phys. **69**, 865 (1997).
[7] S. J. Leib and M. E. Goldstein, Phys. Fluids **29**, 952 (1986).
[8] W. van Saarloos, Phys. Rev. A **39**, 6367 (1989).
[9] W. van Saarloos, Phys. Rev. A **37**, 211 (1988).
[10] P. Huerre and P. A. Monkewitz, Annu. Rev. Fluid Mech. **22**, 473 (1990).
[11] M. Chomaz, Annu. Rev. Fluid Mech. **37**, 357 (2005).
[12] I. Vihinen, A. M. Honohan, and S. P. Lin, Phys. Fluids **9**, 3117 (1997).
[13] A. P. R. Edwards, B. P. Osborne, J. M. Stoltzfus, and T. A. Steinberg, Phys. Fluids **14**, 3432 (2002).
[14] M. Gordillo, J. N. Pérez-Saborid, and A. M. Gañán-Calvo, J. Fluid Mech. **23**, 448 (2001).
[15] A. Sevilla, M. Gordillo, and C. Martinez-Bazán, Phys. Fluids **14**, 3028 (2002).
[16] M. Gordillo, Z. Cheng, A. M. Gañán-Calvo, M. Marquez, and D. A. Weitz, Phys. Fluids **16**, 2828 (2004).
[17] A. Sevilla, M. Gordillo, and C. Martinez-Bazán, Phys. Fluids **17**, 018105 (2005).
[18] A. M. Gañán-Calvo and P. Riesco-Chueca, J. Fluid Mech. **75**, 553 (2006).
[19] A. M. Gañán-Calvo, M. A. Herrada, and P. Garstecki, Phys. Rev. Lett. **96**, 124504 (2006).
[20] A. S. Utada, A. Fernandez-Nieves, J. M. Gordillo, and D. A. Weitz, Phys. Rev. Lett. **100**, 014502 (2008).
[21] P. Guillot, A. Colin, A. S. Utada, and A. Ajdari, Phys. Rev. Lett. **99**, 104502 (2007).
[22] T. M. Squires and S. R. Quake, Rev. Mod. Phys. **77**, 977 (2005).
[23] T. Thorsen, S. J. Maerkl, and S. R. Quake, Science **298**, 580 (2002).
[24] H. Song, D. L. Chen, and R. F. Ismagilov, Angew. Chem., Int. Ed. **45**, 7336 (2006).
[25] T. Thorsen, R. W. Roberts, F. H. Arnold, and S. R. Quake, Phys. Rev. Lett. **86**, 4163 (2001).
[26] S. L. Anna, N. Bontoux, and H. A. Stone, Appl. Phys. Lett. **82**, 364 (2003).
[27] D. R. Link, S. L. Anna, D. A. Weitz, and H. A. Stone, Phys. Rev. Lett. **92**, 054503 (2004).
[28] P. Garstecki, I. Gitlin, W. DiLuzio, E. Kumacheva, H. A. Stone, and G. M. Whitesides, Appl. Phys. Lett. **85**, 2649 (2004).
[29] P. Garstecki, H. A. Stone, and G. M. Whitesides, Phys. Rev.

Lett. **94**, 164501 (2005).
[30] P. Guillot and A. Colin, Phys. Rev. E **72**, 066301 (2005).
[31] A. S. Utada, A. Fernandez-Nieves, H. A. Stone, and D. A. Weitz, Phys. Rev. Lett. **99**, 094502 (2007).
[32] G. Cristobal, L. Arbouet, D. Talaga, J.-L. Bruneel, M. Joanicot, and L. Servant, Lab Chip **6**, 1140 (2006).
[33] P. Guillot, P. Panizza, J.-B. Salmon, M. Joanicot, A. Colin, C.-H. Bruneau, and T. Colin, Langmuir **22**, 6438 (2006).
[34] P. Laval, N. Lisai, J.-B. Salmon, and M. Joanicot, Lab Chip **7**, 829 (2007).
[35] P. Laval, J.-B. Salmon, and M. Joanicot, J. Cryst. Growth **303**, 622 (2007).
[36] D. C. Duffy, J. C. McDonald, O. J. A. Schueller, and G. M. Whitesides, Anal. Chem. **70**, 4974 (1998).
[37] A. M Gañán-Calvo, Phys. Rev. E **75**, 027301 (2007).
[38] K. B. Migler, Phys. Rev. Lett. **86**, 1023 (2001).
[39] A. Frischknecht, Phys. Rev. E **58**, 3495 (1998).
[40] T. R. Powers and R. E. Goldstein, Phys. Rev. Lett. **78**, 2555 (1997).
[41] T. R. Powers, D. Zhang, R. E. Goldstein, and H. A. Stone, Phys. Fluids **10**, 1052 (1998).
[42] M. San Miguel, M. Grant, and J. D. Gunton, Phys. Rev. A **31**, 1001 (1985).
[43] B. Dollet, W. van Hoeve, J.-P. Raven, P. Marmottant, and M. Versluis, Phys. Rev. Lett. **100**, 034504 (2008).
[44] E. Guyon, J.-P. Hulin, L. Petit, and C. D. Mitescu, *Physical Hydrodynamics* (Oxford University Press, Oxford, 2001).
[45] R. B. Bird, W. E. Stewart, and E. N. Lightfoot, *Transport Phenomena* (Wiley, New York, 2002).
[46] R. Eymard, T. Gallouët, and R. Herbin, in *The Finite Volume Method*, edited by Ph. Ciarlet and J. L. Lions , Vol. 7 of Handbook of Numerical Analysis (North Holland, Amsterdam, 2000), pp. 715–1022.